1   # Enhanced diapycnal mixing by polarity-reversing internal solitary

2   # waves in the South China Sea

3   Yi Gong[1], Haibin Song[1]*, Zhongxiang Zhao[2], Yongxian Guan[3], Kun Zhang[1], Yunyan Kuang[1],
4   Wenhao Fan[1]

5   1 State Key laboratory of Marine Geology, School of Ocean and Earth Science, Tongji University, Shanghai 200092,

6   China

7   2 Applied Physics Laboratory, University of Washington, Seattle, WA, USA

8   3 MNR Key Laboratory of Marine Mineral Resources, Guangzhou Marine Geological Survey, China Geological

9   Survey, Guangzhou 510760, China

10   *Corresponding author. hbsong@tongji.edu.cn

11

12   **Abstract**

13   Shoaling internal solitary waves near the Dongsha Atoll in the South China Sea dissipate their
14   energy and thus enhance diapycnal mixing, which have an important impact on the oceanic
15   environment and primary productivity. The enhanced diapycnal mixing is patchy and instantaneous.
16   Evaluating its spatiotemporal distribution requires comprehensive observation data. Fortunately,
17   seismic oceanography meets the requirements, thanks to its high spatial resolution and large spatial
18   range. In this paper, we studied three internal solitary waves in reversing polarity near the Dongsha
19   Atoll, and calculated the spatial distribution of resultant diapycnal diffusivity. Our results show that
20   the average diffusivities along three survey lines are two orders of magnitude larger than the open-
21   ocean value. The average diffusivity in the internal solitary wave with reversing polarity is three
22   times that of the non-polarity-reversal region. The diapycnal diffusivity is higher at the front of one
23   internal solitary wave, and gradually decreases from shallow to deep water in the vertical direction.
24   Our results also indicates that (1) the enhanced diapycnal diffusivity is related to reflection seismic
25   events; (2) convective instability and shear instability may both contribute to the enhanced diapycnal
26   mixing in the polarity-reversing process; and (3) the difference between our and previous diffusivity
27   profiles is about 2-3 orders of magnitude, but their vertical distribution is almost the same.

28

29   [Key words] Internal solitary waves, Polarity reversal, Diapycnal mixing, Northeastern South China
30   Sea, Seismic oceanography.

31

32   **1. Introduction**

33   Energy dissipation of internal waves enhances diapycnal mixing, and turbulence in the form of
34   internal wave breaking is the primary mechanism for mixing thermodynamic properties in the ocean
35   (St. Laurent et al., 2011). Small-scale changes of topography also significantly enhances local
36   mixing (Nash and Moum, 2001; Klymak et al., 2008; Palmer et al., 2013; Staalstrøm et al., 2015;
37   Wijesekera et al., 2020; Voet et al., 2020). Internal tides and internal waves are ubiquitous on the
38   global continental shelves and slopes (Holloway et al., 2001). They play an important role in the
39   global oceanic energy balance and provide energy for ocean mixing (Mackinnon and Gregg, 2003).
40   Due to shoaling internal waves and seafloor roughness, turbulent mixing on the continental shelves

41   and slopes is more variable than in the open ocean (Carter et al., 2005). Diapycnal diffusivity
42   observed on continental shelf and slope can span four orders of magnitude (Gregg and Özsoy, 1999;
43   Nash and Moum, 2001). Internal solitary wave is a kind of nonlinear internal wave, which usually
44   carries a large amount of energy. Numerical simulation results indicate that up to 73% of the internal
45   wave field energy may be in internal solitary waves (Bogucki et al., 1997). Therefore, internal
46   solitary waves propagating to the continental shelf and slope can greatly change the local mixing. A
47   number of researches have been carried out on mixing caused by internal solitary waves on the
48   continental shelf and slope. Observations have shown that the turbulence induced by shear
49   instability at the rear of internal solitary wave sharply increases the mixing (Sandstrom et al., 1989;
50   Sandstrom and Oakey, 1995; Moum et al., 2003; Richards et al., 2013). Mackinnon and Gregg (2003)
51   estimated that 50% of the dissipation in the thermocline occurred during the propagation of internal
52   solitary waves according to their observations. The elevation internal solitary waves propagating
53   near the seafloor enhances mixing, resuspending and transporting materials, which has an important
54   impact on the local ecological environment (Klymak and Moum, 2003; Moum et al., 2007).

56   Internal solitary waves are ubiquitous in the northeastern South China Sea (Zhao et al., 2003;
57   Klymak et al., 2006; Xu et al., 2010; Cai et al., 2012; Alford et al., 2015). They are generated by
58   interaction of internal tides and topography in the Luzon Strait and propagate toward Dongsha Atoll,
59   where their energy is dissipated in shoaling. The continental shelf and slope of the northeastern
60   South China Sea is close to the source, so that the amplitude and energy of internal solitary waves
61   in this area are large. The energy dissipation of internal solitary waves occurs most near Dongsha
62   Atoll and its southeastern shelf (Lien et al., 2005; Chang et al., 2006; St. Laurent, 2008).
63   Observations show that high turbulence mainly occurs in the continental shelf region, and the
64   average diffusivity can reach the order of O(-3) m2 s-1, while the diffusivity in the continental slope
65   region is one order of magnitude lower (Yang et al., 2014). When nonlinear internal waves travel
66   cross the continental slope, the waveform changes into different types (Terletska et al., 2020). In
67   this process, mixing is enhanced, and about 30% of the energy dissipation occurs near the seafloor
68   (St. Laurent, 2008). The energy flux of internal solitary waves around the Dongsha Plateau is large.
69   Lien et al. (2005) estimated that, if all nonlinear internal waves break within water depth of 10 m
70   and in a range of 200×200 km^2 centered on Dongsha Plateau, the magnitude of diffusivity can
71   exceed an order of O(-3). In addition, internal solitary waves shoaling near the Dongsha Atoll also
72   dissipate a lot of energy and improve the local mixing efficiency (Orr and Mignerey, 2003; St.
73   Laurent et al., 2011). The water in the northeastern South China Sea can exchange heat with the
74   water in the Pacific Ocean through the Kuroshio, and heat can be transferred to atmosphere through
75   the sea-air interface on the continental shelf as well. Therefore, internal solitary waves are an
76   important link for energy transfer in the South China Sea and play an important role in our
77   understanding of energy transfer between the ocean and climate environment.

79   Turbulence in the ocean is patchy and instantaneous. Therefore, it requires extensive observations
80   to accurately evaluate turbulent mixing (Whalen et al., 2012; Waterhouse et al., 2014; Kunze, 2017).
81   Seismic oceanography (Holbrook et al., 2003) has the advantages of wide observation range and
82   high spatial resolution (Ruddick et al., 2009), which is suitable for observing the spatial distribution
83   of turbulent mixing. Sheen et al. (2009) used reflection seismic data to give a diffusivity section of
84   oceanic front in the South Atlantic. Holbrook et al. (2013) comprehensively introduced the

Nonlinear Processes
in Geophysics
Discussions

85 theoretical basis for evaluating turbulent mixing from reflection seismic data. Subsequently, a large
86 number of scholars have used the reflection seismic method to study the spatial distribution of
87 turbulent mixing in different ocean regions or turbulent mixing induced by different ocean
88 phenomena (Fortin et al., 2016; Sallares et al., 2016; Dickinson et al., 2017; Mojica et al., 2018).
89
90 In this article, we used two-dimensional seismic data to observe the propagation of internal solitary
91 waves near the Dongsha Atoll, and calculated the spatial distribution of local diapycnal diffusivity
92 to evaluate the impact of internal solitary wave shoaling on turbulent mixing. Section 2 introduces
93 seismic data processing and the method of calculating turbulence mixing parameters. Section 3
94 describes the polarity reversal of internal solitary waves, horizontal slope spectrum and distribution
95 of turbulence diffusivity. In section 4 we analyze the relationship between diapycnal diffusivity and
96 reflection seismic events, and discuss the mechanism of turbulent mixing induced by internal
97 solitary waves. Besides, we compare the mixing scheme with our results. Section 5 gives a summary.
98
99 **2. Data and methods**
100 **2.1. Seismic data acquisition and processing**
101
102 The water is shallow on the continental shelf and slope near the Dongsha Atoll, so internal solitary
103 waves reach the transition point and their polarity changes from depression to elevation. In the
104 summer of 2009, the Guangzhou Marine Geological Survey (GMGS) set up a two-dimensional
105 seismic observation network in the Dongsha area. We found three internal solitary waves during the
106 polarity reversal process on the L1, L2, and L3 survey lines of the seismic data. The survey lines
107 are shown in Figure 1a, b. The streamer used in the acquisition process has a total length of 6 km
108 and 480 channels, the trace interval is 12.5 m, and the sampling interval is 2 ms. The airgun source
109 capacity is 5080 in^3 (1 in=2.54 cm), and the main frequency of the source is 35 Hz. The shot interval
110 is 25 m, and the minimum offset is 250 m. The time interval of shots is about 10 s. Survey lines L1
111 and L2 are the in-lines, which were from the southeast to the northwest. Survey line L3 is a cross-
112 line, which was from the southwest to the northeast. We calculated the mean buoyancy frequency
113 (Figure 1c) of the region around seismic survey lines (latitude range 21.5°-22.5°, longitude range
114 116°-118°, blue box in Figure 1a) by reanalysis temperature and salinity data with a water depth of
115 100-350 m. This depth range matches the observation depth of the seismic data. The hydrographic
116 data are provided by Copernicus Marine Environment Monitoring Service (CMEMS).
117
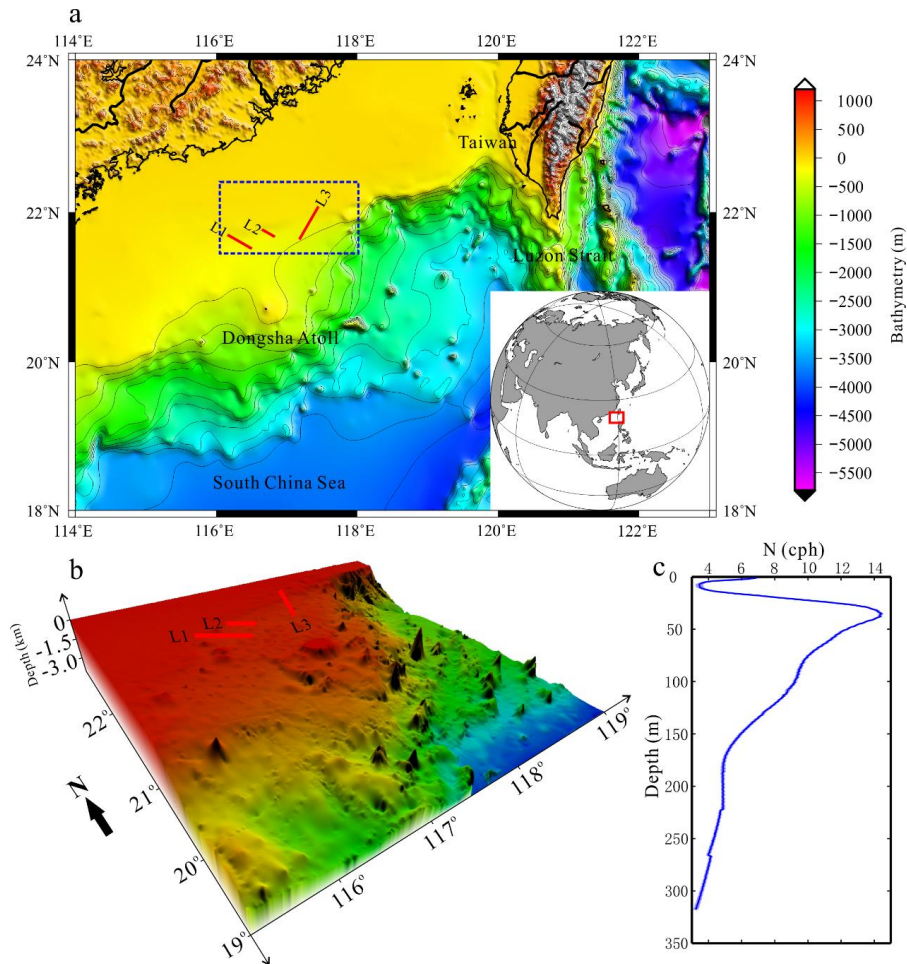
Figure 1. Bathymetry of the Dongsha area and the locations of seismic survey lines. (a) 2D bathymetry map of the northeastern of South China Sea, with the red lines representing the seismic survey lines. (b) 3D bathymetry map around the Dongsha Atoll. (c) The mean buoyancy frequency around seismic survey lines (blue box in (a)) and its 95% confidence interval (blue shadow).

After a conventional processing of the seismic data, an image of the ocean interior's structure can be obtained. This image can be approximated as a temperature or salinity gradient map of the water column (Ruddick, et al., 2009). The conventional processing of seismic data has 5 main steps, including defining the observation system, noise and direct wave attenuation, velocity analysis, normal moveout (NMO) and horizontal stacking. Then we use a bandpass filter to filter out low-frequency noise below 8 Hz and high-frequency noise above 80 Hz. According to the linear characteristics of the direct wave, we use a median filter to extract the direct wave signal, and subtract it from the original signal to achieve the purpose of attenuating the direct wave. Subsequently, we sorted the seismic data from shot gathers into common midpoint gathers (CMPs). Sound speed is a function of depth and obtained through velocity analysis, and then the NMO is

134   applied to CMPs according to the function to flatten the reflection seismic events of the water
135   column. When NMO is applied, the seismic wave with large offset will be stretched, and the
136   stretched seismic waves need to be cut off. Usually, the default method is to use a linear function to
137   remove the stretched seismic waves (Figure 2a). This may lose a lot of shallow reflection signals
138   (Figure 2b). Bai et al. (2017) used the common offset seismic section to supplement the missing
139   information in shallow water, but the low signal-to-noise ratio of the common offset seismic section
140   cannot guarantee the imaging quality. In order to retain more shallow reflection signal, we used a
141   custom function to cut off the NMO stretch (Figure 2c), thereby satisfying the imaging requirement
142   of the shallow water column (Figure 2d). Finally, the seismic section of the water column can be
143   obtained by stacking the processed CMPs. Due to the shallow water depth, the seismic data is
144   seriously affected by swell noise. We filtered out the components of stacked seismic data in wave
145   number range corresponding to swells in the frequency-wave number domain. A detailed description
146   of the seismic data processing can be found in Ruddick et al. (2009).

147
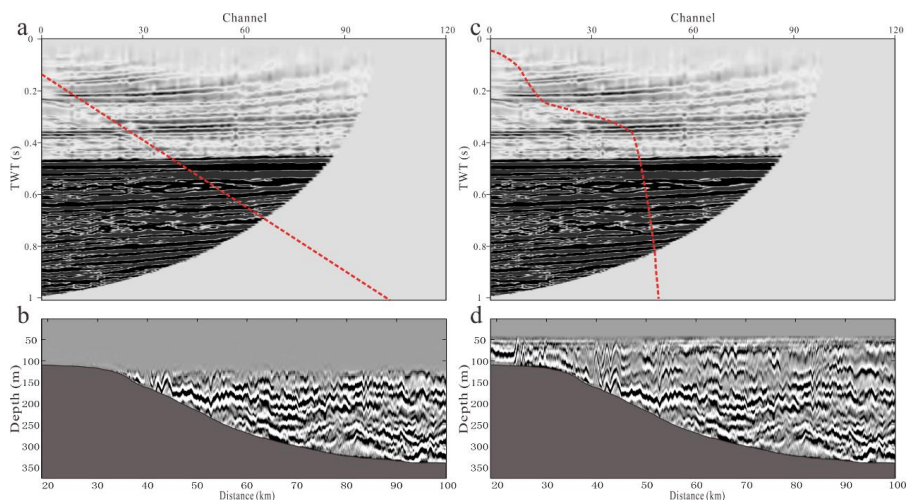
148

149   Figure 2. Cutting off the stretch of NMO with a linear function (a) and the corresponding seismic section
150   (b). Cutting off the stretch of NMO with a custom function (c) and the corresponding seismic section (d).
151   The red dotted line shows the cut off trace, the right part of seismic data is cut off. The unit TWT of (a)
152   and (b) is the two-way travel time of seismic wave from source to receiver.

153

154   **2.2. Diapycnal diffusivity estimates from seismic data**

155

156   Klymak and Moum (2007b) found that the horizontal wavenumber spectrum of the vertical
157   isopycnal displacement can be interpreted as the internal wave spectrum at low wavenumbers and
158   the turbulence spectrum at high wavenumbers. The high wavenumber components of spectrum are
159   dominated by turbulence, and the spectral energy follows the -5/3 power of the wavenumber. The
160   turbulence part of the horizontal wavenumber spectrum can be expressed by a simplified Batchelor
161   model (Equation 2-1), so the turbulence dissipation ε can be estimated from the observed
162   horizontal wavenumber spectrum. And diapycnal diffusivity can be calculated from Equation 2-2
163   (Osborn, 1980).

164 $$\phi_\zeta^T = \frac{4\pi\Gamma}{N^2} C_T \varepsilon^{\frac{2}{3}} (2\pi k_x)^{-\frac{5}{3}} \tag{2-1}$$

165 $$K_\rho = \Gamma\varepsilon / N^2 \tag{2-2}$$

166 Where ϕ_ζ^T represents horizontal wavenumber spectrum, $\Gamma = 0.2$ is the mixing coefficient, N

167 is the buoyancy frequency, $C_T = 0.4$ is the Kolmogorov constant, ε represents the turbulence

168 dissipation, k_x is the horizontal wavenumber, and K_ρ represents the diapycnal diffusivity.

169

170 Observations (Nandi et al., 2004; Nakamura et al., 2006; Sallarès et al., 2009) and simulations
171 (Holbrook et al., 2013) show that the reflection seismic events and isopycnal are spatially consistent.
172 Therefore, the horizontal wavenumber spectrum calculated from the vertical displacement of the
173 reflection seismic events is equivalent to the horizontal slope spectrum that Klymak and Moum
174 (2007b) calculated from horizontal tow measurements. The turbulence dissipation and diapycnal
175 diffusivity can also be calculated from seismic data (Sheen et al., 2009; Holbrook et al., 2013). First,
176 we use the seismic interpretation software to pick up reflection events in the seismic section (Figure
177 3a). Then we calculate the vertical displacement of the reflection events. The vertical displacement
178 is the distance of the reflection evens deviate from the equilibrium position in the vertical direction.
179 We take the mean water depth of the reflection events as the equilibrium position. Note that the
180 choice of equilibrium position will not affect the calculation result. The spectral energy ϕ_ζ^T of the
181 vertical displacement in the horizontal wavenumber domain can be obtained by Fourier transform.
182 In practical applications, we use the slope spectrum $\phi_{\zeta_x}^T$ instead of the displacement spectrum ϕ_ζ^T
183 to distinguish the turbulence subrange from the internal wave subrange. The spectral slope is as
184 follows (Holbrook et al., 2013):

185 $$\phi_{\zeta_x}^T = (2\pi k_x)^2 \phi_\zeta^T \tag{2-3}$$

186 This conversion changes the wavenumber power law in the turbulence subrange from -5/3 to 1/3,
187 so that it can be distinguished from the internal wave subrange with -1/2 power law (-5/2 in the
188 displacement spectrum). In calculating the turbulence dissipation in the seismic section, it is
189 necessary to grid the section and calculate the dissipation in each grid separately. The horizontal
190 grid is set as 5 km, and the grid step 2.5 km. As the water depth in the seismic data is shallow, the
191 reflection seismic events are less in the vertical direction. In order to ensure more than two events
192 in each grid, we set the vertical grid to be 75 m and the grid step 37.5 m. In each grid, we calculated
193 the spectral slope of each event and took the average as $\overline{\phi_{\zeta_x}^T}$. We fitted the averaged spectrum in
194 the turbulence subrange to the Equation 2-1 and calculated the turbulence dissipation ε. To reduce
195 uncertainty, we only calculated the cases with a length >1000 m in each grid. Experiments showed
196 that this length can correctly represent the slope of energy spectra in turbulence subrange (Figure
197 3b). After traversing all the grids, the turbulent dissipation section is obtained, and the diapycnal
198 diffusivity section can be obtained as well according to Equation 2-2. The uncertainty of the

199   turbulence dissipation and diapycnal diffusivity was evaluated by the error between observed
200   average slope spectrum and the fitted Batchelor model. We used a spline smoothing function to
201   smooth the meshing results.

202

203
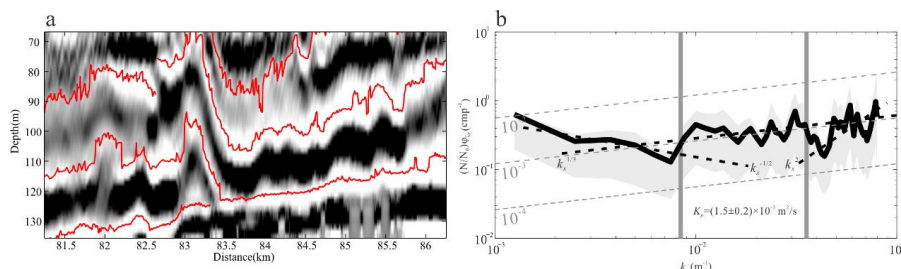
204   Figure 3. (a) The reflection seismic events in a grid. (b) The average horizontal slope spectrum (black
205   line). The gray shadow represents the 95% confidence interval. The gray dashed lines represent the
206   diffusivity contour. The black dashed lines represent the spectral slopes in internal wave subrange,
207   turbulence subrange and noise subrange, respectively. The gray vertical lines indicate the boundaries of
208   turbulence subrange.

209

210   **2.3. Estimating the horizontal wave-induced velocity of internal solitary wave**

211

212   We estimated the wave-induced horizontal velocity of internal solitary wave according to the
213   method proposed by Moum et al. (2007). This method requires observation data to satisfy two
214   assumptions: 1) the isopycnal is parallel to the streamline; 2) the internal solitary wave satisfies the
215   KdV equation. Moum et al. (2007) picked the isopycnal from the high-frequency acoustic section
216   and fitted it with the KdV equation. The displacement equation of isopycnal can be obtained, and
217   the derivation of displacement equation is the wave-induced velocity. Seismic data satisfy the first
218   assumption. Although breaking induced polarity reversal of internal solitary waves close the
219   streamlines, it is difficult to record reflection seismic data from those areas with closed streamline
220   at the resolution scale of seismic data. The regional density gradient recorded by the reflection
221   events still exists, and the streamline is parallel to the isopycnal at this time. While areas with closed
222   streamlines are strongly mixed, and the density gradient weakens or even disappears, which cannot
223   be recorded in seismic data. Unfortunately, the internal solitary waves we observed do not satisfy
224   the second assumption. The KdV equation can simulate internal solitary waves with small amplitude
225   and weak nonlinearity, but the polarity reversal of the large-amplitude internal solitary waves we
226   observed cannot be simulated well. Here we did not use theoretical models to fit observations.
227   Although there are studies using theory to successfully simulate the polarity reversal of internal
228   solitary waves (Liu et al., 1998; Zhao et al., 2003;), it is difficult to match theories and observations.

229   We used the picked reflection seismic events to calculate the isopycnal displacement $\eta(x, z)$

230   (Figure 4b). The $\eta(x, z)$ is the distance that reflection seismic events deviate from the equilibrium

231   position, which is determined by the mean depth of two shoulders of one internal solitary wave

232   (Figure 4a). We smoothed $\eta(x, z)$ with a spline function same as that was used for smoothing

233 turbulence dissipation, so that the resolution of wave-induced velocity is consistent with that of

234 turbulence dissipation. Therefore, the stream function can be expressed as (Holloway et al., 1999):

235 $\Psi(x, z) = c\eta(x, z)$ (2-4)

236 where c is the phase velocity of internal solitary waves. The c can be estimated from pre-stack

237 seismic data (Tang et al., 2014, 2015; Fan et al., 2021). The seismic data is redundant, because we

238 have made multiple observations of the same events, which allows us to study the movement of the

239 water column. Specifically, after sorting the seismic data into CMPs (section 2.1), we extract traces

240 with the same offset from CMPs to form common offset gathers (COGs). Multiple COGs can be

241 obtained in the order of offset from small to large. The larger the offset, the lower the signal-to-

242 noise ratio of the data. We selected the first five COGs to ensure the imaging quality. Pre-stack

243 migration of COGs yields COG sections. These COG pre-stack migration sections show images of

244 the same water column at different times. Tracking the change of shot-receiver pairs at a certain

245 reflection point yields the phase velocity (Fan et a., 2021). Figure 4c shows the change of the shot-

246 receiver pairs of internal solitary wave trough in the L1 survey line. The straight line represents the

247 fitting line of the shot-receiver pairs. The average phase velocity of the internal solitary wave during

248 the imaging time is $c = \dfrac{d_{cmp}}{dt_s} k$, where d_{cmp} is the half of the trace interval, dt_s the time

249 interval of shot, and k the slope of the fitted line. After calculating the flow function according to

250 Equations 2-4, the wave-induced horizontal velocity can be expressed as:

251      $u(x, z) = \dfrac{\partial \Psi}{\partial z}$ (2-5)

252
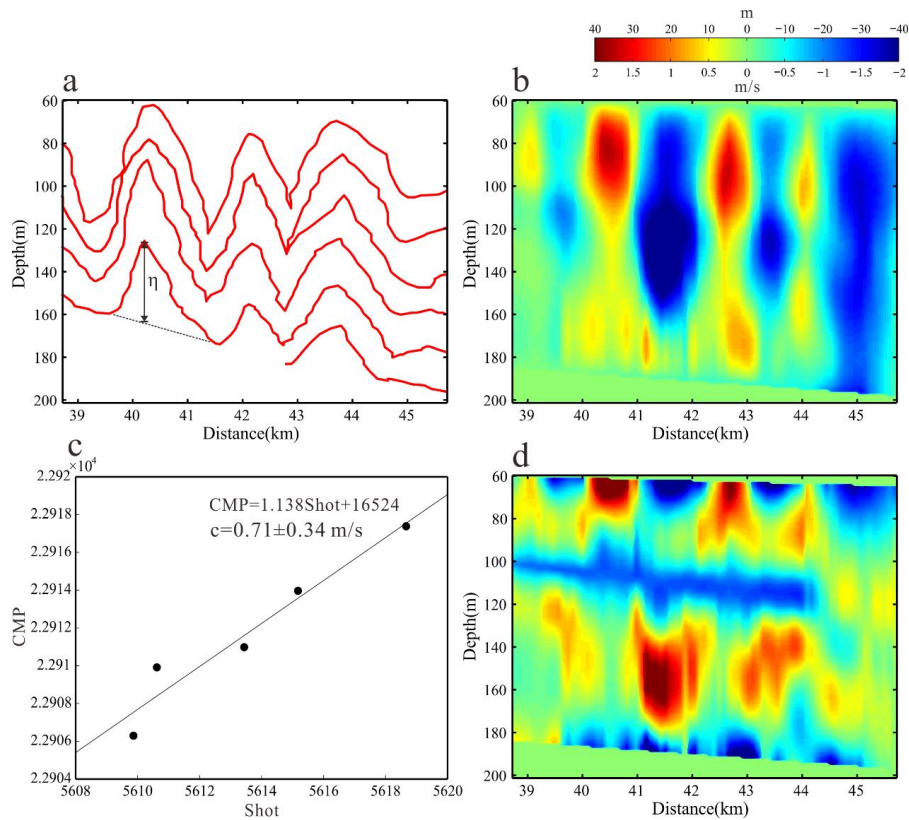
Figure 4. (a) Schematic of calculating internal solitary wave isopycnal displacement using reflection seismic events. (b) The isopycnal displacement section of internal solitary wave. (c) Calculating the mean phase velocity of internal solitary wave by pre-stack seismic data. (d) The wave-induced horizontal velocity.

Note that the wave-induced velocity here is in the seismic resolution scale, which can be regarded as its low-frequency component only. The results are insufficient to characterize the high-frequency components. But such rough wave-induced velocity is useful, because the purpose of calculating wave-induced velocity is for the vertical mixing scheme. The wave-induced velocity makes the resolution scale of the mixing scheme equal to that of mixing parameters estimated from the seismic data, and the two are comparable. In addition, the error of the wave-induced velocity is mainly determined by the error of the phase velocity of the internal solitary wave. For internal solitary waves with polarity reversal, the error of the phase velocity is large, because the phase velocity gradually decreases when the internal solitary wave is shoaling (Bourgault et al., 2007; Shroyer et al., 2008). It can be seen from Figure 4c that the shot-receiver pairs do not completely fall on the fitted line.

2.4. Mixing scheme for internal solitary waves shoaling

273   Shoaling and breaking of internal solitary waves on the continental shelf and slope enhance mixing.

274   Vlasenko and Huntter (2002) studied the breaking of internal solitary waves over slope-shelf

275   topography by numerical simulation. In their model, the mixing scheme (PP scheme) proposed by

276   Pacanowski and Philander (1981) was improved, and a vertical mixing scheme for resolving

277   breaking internal solitary waves was given. In this scheme, the vertical turbulence kinematic

278   viscosity and diffusivity are determined by the Richardson-number-dependent turbulence

279   parameterizations. The expression is as follows:

280 $$Ri = \frac{N^2}{u_z^2} \tag{2-6}$$

281 $$\nu = \frac{\nu_0}{(1+\alpha Ri)^n} + \nu_b \tag{2-7}$$

282 $$\kappa = \frac{\nu_0}{(1+\alpha Ri)^n} + \kappa_b \tag{2-8}$$

283   Where u_z is the vertical gradient of horizontal wave-induced velocity, ν is vertical turbulence

284   kinematic viscosity, κ is vertical turbulence kinematic diffusivity. Vlasenko and Huntter (2002)

285   selected the best model parameters after a series of experiments. They are $\nu_0 = 10^{-3} m^2 s^{-1}$,

286    $\nu_b = 10^{-5} m^2 s^{-1}$, $\kappa_b = 10^{-6} m^2 s^{-1}$, $\alpha = 5$ and $n = 1$. Based on this model, they simulated the

287   process of internal solitary wave shoaling and breaking on slope-shelf topography and studied the

288   breaking criterion.

289

290   **3. Results**

291   **3.1. Polarity reversal of internal solitary wave in seismic section**

292

293   When one internal solitary wave propagates cross the transition point, it converts from a depression

294   wave to an elevation wave. In the two-layer ocean model, the transition point is defined as the

295   position where the pycnocline is close to the mid-depth (Grimshaw et al., 2010). The three seismic

296   sections in Figure 5 capture the images of internal solitary waves passing the transition point. Figure

297   5a is the seismic section of survey line L1. It shows that the water depth becomes shallower from

298   southeast to northwest, and the bottom slope is steeper between 30-60 km. In the deep-water region

299   of 60-100 km, internal waves are developed, and the reflection seismic events fluctuate obviously.

300   Near the seafloor around 80 km, the reflection seismic events are uplifted and discontinuous,

301   forming a fuzzy reflection area. A mode-1 depression internal solitary wave can be identified at 53

302   km, indicating that the transition point has not been reached yet. The internal solitary wave has

303   reversed polarity in the area of 40 km, and a packet of three elevation waves is formed during the

304   polarity reversal process. The reflection seismic events is continuous here, and no obvious wave

305   breaking is found. Five elevation waves can be identified around 24-37 km, among which four

306   elevation waves at 24 km may be formed continuously, while the elevation wave at 37 km formed

307   later.

308

309   Figure 5b gives another internal solitary wave polarity reversal process captured by the survey line
310   L2. There are two obvious depression waves at 16 km. There are multiple waves with smaller
311   amplitude around 10-15 km. The polarity of internal solitary wave is reversing within 4-8 km. The
312   length of the head wave becomes wider and the slope becomes gentler. The leading wave is followed
313   by a packet of   multiple elevation waves. The reflection seismic events are continuous in the whole
314   section.

315

316   L3 is a cross line whose observation direction is perpendicular to survey line L1 and L2 (Figure 5c).
317   There are multiple depression waves with large amplitude around 20-35 km, and the reflection
318   seismic events are continuous. The wave polarity is reversing within 10-20 km, and the reflection
319   seismic events are discontinuous in this region. At 10 km, there is a large-amplitude elevation
320   internal solitary wave, and the wave front is almost parallel to seafloor. There is a large-amplitude
321   depression wave at 17 km, and the wave trough has interacted with topography. The reflection
322   seismic events before 10 km are discontinuous, and the events near the seafloor are fuzzy. It
323   indicates that internal solitary waves break and induce strong mixing during the process.

324
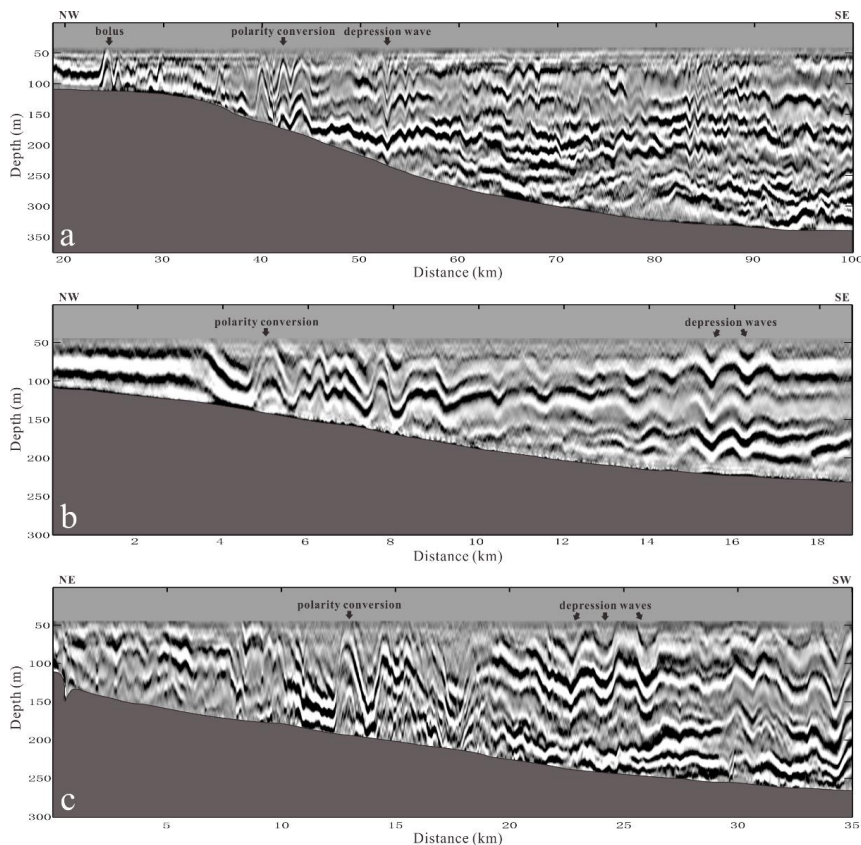
325

326   Figure 5. The seismic sections of survey line L1 (a), L2 (b) and L3 (c). The gray regions in the sections
327   represent seafloor. Internal solitary waves can be clearly seen in all three cases.

328

3.2. The horizontal slope spectrum

330

331   We picked the reflection seismic events in the three sections (Figure 7) and calculated the horizontal
332   slope spectrum using the method described in section 2.2. Figure 6 shows the average horizontal
333   slope spectrum of the three sections. We calculated the horizontal slope spectrum of all tracked
334   events and averaged in logarithmic space to determine the wavenumber of turbulence subrange. The
335   turbulence subrange of the survey line L1 section is 0.005-0.069 m^{-1}, as shown by the gray vertical
336   line in Figure 6a. The corresponding wavelength is 15-200 m. The average diapycnal diffusivity is
337    $(7.0 \pm 1.2) \times 10^{-4}$ m^2/s, which is one order of magnitude larger than the open-ocean value (10^{-5} m^2/s).
338   The spectral energy in internal wave subrange is larger than that in turbulence subrange, indicating
339   that the energy is dominated by internal waves. This is confirmed by internal waves in the seismic
340   sections. The difference from Holbrook et al. (2013) is that the calculated horizontal slope spectrum
341   does not include harmonic noise. This may be because the harmonic noise has been removed when
342   we filtered the swell noise. In addition, we have not smoothed the events, so some high wavenumber
343   ranges are reserved. If the events are smoothed, the spectral energy will decrease rapidly in the high
344   wavenumber range (Holbrook et al., 2013; Tang et al., 2019).

345

346   The horizontal slope spectrum of the L2 section is shown in Figure 6b. The turbulence subrange is
347   0.008-0.068 m^{-1}, and the corresponding wavelength is 15-133 m. Compared with the survey line L1,
348   the turbulence shifts to a smaller scale. The spectral energy in internal wave subrange has the same
349   order of magnitude as the spectral energy in turbulence subrange, which indicates that the energy is
350   transferring to small-scale turbulence. This process is closely related to the polarity reversal of
351   internal solitary waves. The average diapycnal diffusivity is $(1.5 \pm 0.1) \times 10^{-3}$ m^2/s, which is two
352   orders of magnitude larger than the background value.

353

354   Figure 6c is the horizontal slope spectrum of the L3 section. It can be seen from the spectrum that
355   the turbulence subrange is small, ranging from 0.011-0.07 m^{-1}. The corresponding wavelength scale
356   is 14-89 m. The internal wave energy is larger and occupies a larger scale range. It can be seen from
357   the seismic section of survey line L3 (Figure 5c) that the amplitudes of the internal waves are large.
358   It indicates that the internal waves carry more energy, so the spectral energy in internal wave
359   subrange is larger (Figure 6c). In addition, there are many discontinuous and weak reflections in the
360   seismic section caused by breaking internal solitary waves. Internal solitary wave breaking weakens
361   the density gradient and enhances local mixing. This phenomenon is most obvious in the survey line
362   L3, where the average diffusivity is the largest of the three sections, $(2.2 \pm 0.2) \times 10^{-3}$ m^2/s.

363
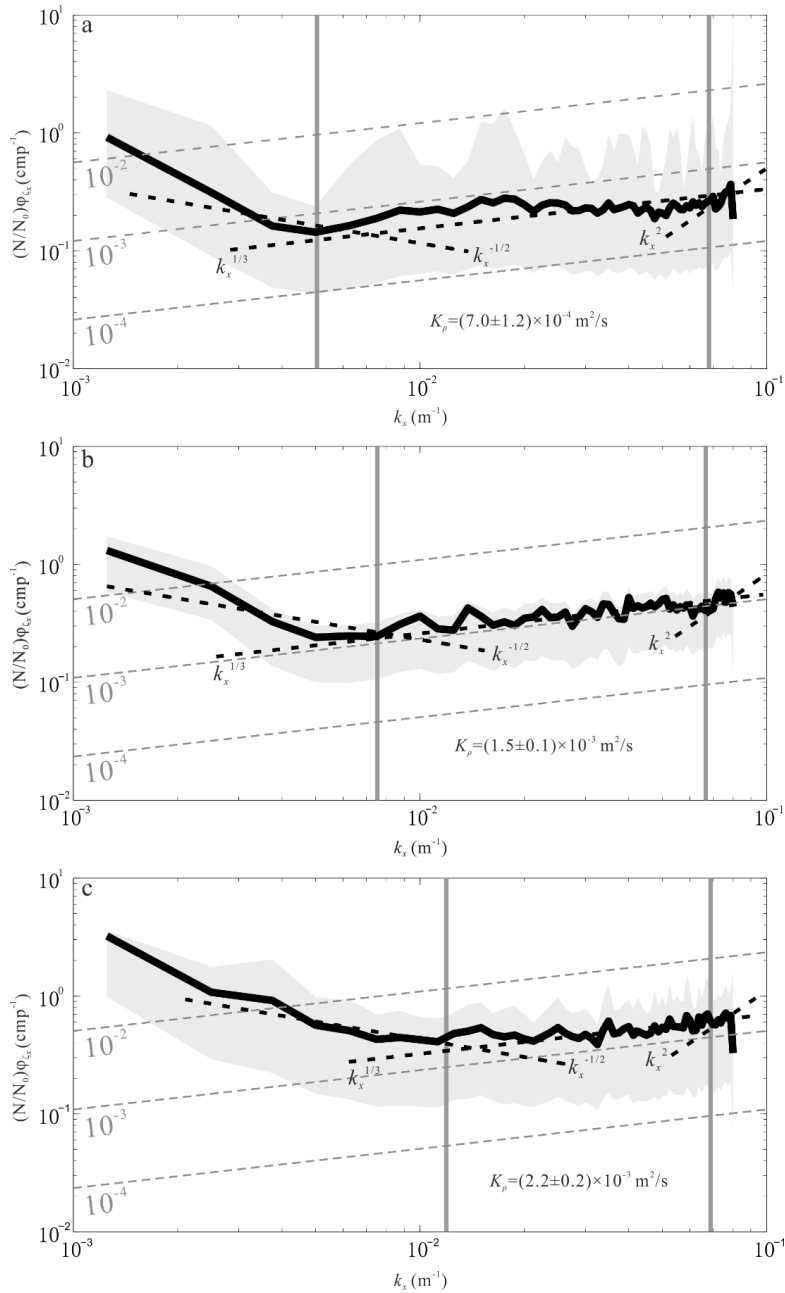
Figure 6. The average horizontal slope spectrum of L1 section (a), L2 section (b) and L3 section (c). The black line is the spectrum, the gray shadow represents the 95% confidence interval, the gray dashed lines represent the diffusivity contour, the black dashed lines represent the spectral slopes in internal wave subrange, turbulence subrange and noise subrange, respectively. The gray vertical lines represent the boundaries of turbulence subrange.

370

371 Figure 6 shows that the spectral energy of the L1 section is smaller than that of the other two sections.
372 This may be because the imaging range of the L1 section is different. The observations in the L2
373 and L3 sections are the polarity reversal of internal solitary waves, while the L1 section includes
374 not only the polarity reversal process, but also internal waves in deep water. The spectral energies
375 of these two processes should be different. We calculated the average horizontal slope spectrum of
376 the polarity reversal region and the non-polarity reversal region, respectively (Figure 7). The
377 spectral energy of the polarity reversal region in L1 section is higher than that of the non-polarity
378 reversal region, so does diapycnal diffusivity (Figure 7a). It implies that the wave energy will
379 accelerate to dissipate and transfer to turbulence when its polarity is reversed. Compared with the
380 non-polarity reversal region, the turbulence subrange of the polarity reversal region is smaller. The
381 lower boundary of the turbulence subrange of the polarity reversal region is slightly larger than that
382 of the non-polarity reversal region. It indicates that the turbulence in this region has a smaller scale.
383 The diapycnal diffusivity in the polarity reversal region in L2 section is about 3 times that of the
384 non-polarity reversal region (Figure 7b). The turbulence subrange of the polarity reversal region in
385 L2 section is slightly larger than that of the non-polarity reversal region. From the L2 section, it can
386 be seen that the events are continuous during the polarity reversal process, which indicates that the
387 wave breaking is weak. The internal solitary wave gradually fissions into several tails during the
388 polarity reversal, and energy is dissipated constantly. Therefore, there will be a large turbulence
389 subrange in the lateral direction (Figure 7b). This process can dissipate much more energy compared
390 with direct breaking of internal solitary waves (Masunaga et al., 2019). The diapycnal diffusivity in
391 the polarity reversal region in L3 section is larger, more than 3 times that of the non-polarity reversal
392 region. Although there are more internal (solitary) waves with larger amplitude in the non-polarity
393 reversal region, the diapycnal diffusivity is lower. The polarity reversal of internal solitary waves
394 significantly increases the diapycnal diffusivity. The turbulence subrange of the polarity reversal
395 region is small, and the lower boundary of the turbulence subrange is greater than 0.01 m^{-1}.

396
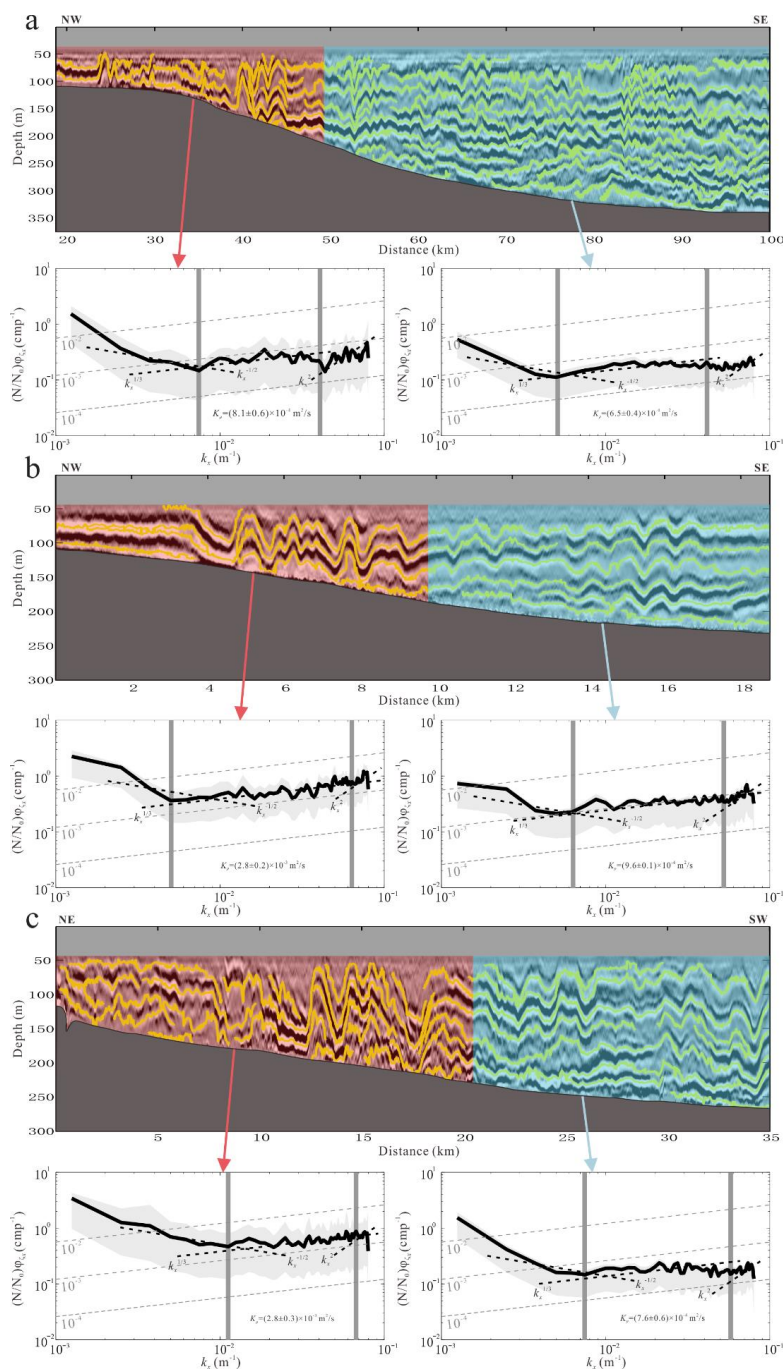
Figure 7. The horizontal slope spectra of the polarity reversal and non-polarity reversal regions calculated from L1 section (a), L2 section (b) and L3 section. The yellow lines are tracked reflection seismic events.
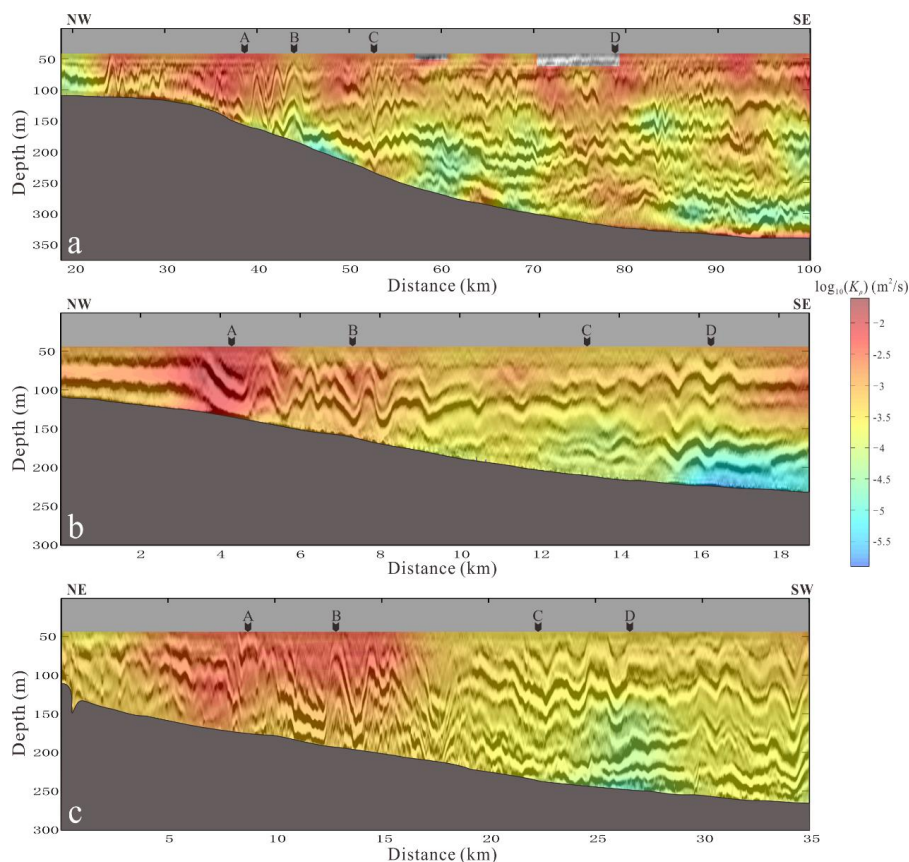
3.3. Diapycnal diffusivity maps

The diapycnal diffusivity maps of the three survey lines are shown in Figure 8. Figure 8a shows the map of the survey line L1. The diffusivity is higher than that of the open ocean. The high value presents a patchy distribution, mainly distributed in the depth between 50-150 m. The low diffusivity values are mainly distributed in the depth between 150-300 m. Some high values are also distributed near the seafloor. The diffusivity is larger in the polarity reversal region (24-45 km). Compared the diffusivity of the four adjacent elevation internal solitary waves (24-30 km), we find that the diffusivity is proportional to the amplitude of internal solitary waves. It means that the large amplitude internal solitary waves contribute more to mixing. In the polarity reversal region (40-45 km), the diffusivity of the head wave's front is higher, that is, where the slope of the wave front becomes gentle. While the diffusivity of the two elevation waves followed the head wave is small. It indicates that the mixing induced by the internal solitary wave polarity reversal is stronger at the beginning, and more energy is dissipated at this time. In the non-polarity reversal region (50-100 km), the diffusivity is low. The mode-1 depression internal solitary wave at 52 km increases the diffusivity. There is an abnormal reflection area near the seafloor at 80 km, and the diffusivity is high. In addition, there is also an area with increased diffusivity between 100-250 m at 93 km. This may be related to the activity of large amplitude internal waves.

The diffusivity map of the survey line L2 is shown in Figure 8b. The high value is mainly distributed at the front of head wave during polarity reversal process (4 km), which is consistent with the characteristics on L1. The diffusivity after the head wave is low, but it is still higher than that in other regions. The diffusivity in the non-polarity reversal region is almost uniform. The two internal solitary waves at 15-16 km did not increase the diffusivity. There is a low diffusivity area near the seafloor around 16-18 km, which is caused by not tracked reflection seismic events in this area. The diffusivity map of survey line L3 (Figure 8c) is similar to that of L2. The high value is distributed in the polarity reversal region and the diffusivity of head wave is still high. However, unlike the diffusivity map of L2, the high diffusivity is mainly distributed in the shallow part of the head wave (water depth 50-120 m), while the diffusivity of the whole head wave in L2 is high. In the non-polarity reversal region, the diffusivity is small and the distribution is uniform too. The diffusivity near the seafloor at 25-27 km is slightly lower than other regions.

Figure 8. The diapycnal diffusivity map of survey line L1 (a), L2 (b) and L3 (c). The black arrows represent the position of vertical diffusivity profile.

4. Discussions

4.1 The relationship between diffusivity and reflection seismic events

When there is a significant impedance difference in the water column, a reflection seismic event will occur (Holbrook et al., 2003; Ruddick et al., 2009). The impedance difference in the ocean is contributed by temperature gradient and salinity gradient, where the former is usually greater than the latter (Ruddick et al., 2009; Sallarès et al., 2009). Density is a function of temperature and salinity, so the reflection seismic events are related to the density gradient. The enhanced mixing reflects the structure of density gradient, thereby changing the appearance of the reflection seismic events. Understanding the relation between diffusivity and reflection seismic events can help us analyze the spatial distribution of diapycnal mixing by seismic section. Figure 8 shows that the reflection seismic event in the high diffusivity region is obviously different from that in the low diffusivity region. In the high diffusivity area (red in Figure 8), the reflection seismic events are fuzzy, discontinuous or bifurcate. While in the low diffusivity area (yellow and blue in Figure 8), the reflection seismic events are clear and continuous. This is because regions with high diffusivity

452 are strongly mixed. The density gradient is changed by mixing, so that it affects the appearance of
453 reflection seismic events. For example, in the polarity reversal region of three seismic sections, the
454 diffusivity is high, and the reflection seismic events are fuzzy and discontinuous. Especially in the
455 range of 5-10 km in Fig. 8c, the events are obviously break and weak. The diffusivity is low in areas
456 where the events are clear, such as the region near the seafloor around 45-50 km and the region near
457 the sea floor around 93-99 km in Figure 8a, and the region near the sea floor around 24-27 km in
458 Figure 8c.

459

460 The diffusivity is not only related to the continuity of the reflection events, but also related to the
461 fluctuation intensity of the events. The greater the fluctuation intensity of the events, the higher the
462 spectral energy, and the greater the diffusivity value. There is a mode-1 depression internal solitary
463 wave at 50-58 km in Figure 8a, and the reflection seismic event is clear and continuous at 180 m.
464 But the diffusivity is high, because the reflection events fluctuate more strongly. It can be seen from
465 the figure that, in addition to the amplitude of the internal solitary wave, there are also many high-
466 frequency waves at the shoulders of the internal solitary wave. These waves increase the spectral
467 energy and result in a higher diffusivity. In addition, the reflection seismic events before 4 km in
468 Figure 8b is continuous and without obvious fluctuations, but the diffusivity is higher. It can be seen
469 from the figure that the reflection events of this region are thicker than that of other regions. The
470 seismic data processing of the three sections in Figure 8 is the same, so the thicker events in Figure
471 8b do not stem from the low frequency of seismic waves. We think this may be caused by small-
472 scale mixing between layers, such as K-H instability. Figure 9 is an enlarged view of the location
473 between 2-3 km in the seismic section of L2 (Figure 5b). The wavelength of the seismic wave (red
474 line) at 80 m is larger than that at the seafloor, which is formed by the overlap of multiple wavelets.
475 It can be seen from the figure that a weak reflection event is barely visible at 80 m, which indicates
476 a thin reflection layer with weak impedance differences. The K-H instability can continue for a long
477 distance in the lateral direction (Seim and Gregg, 1994; Haren et al., 2014; Chang et al., 2016; Tu
478 et al., 2019) and enhance local ocean mixing. This structure can form at the tail of internal solitary
479 wave (Moum et al., 2003). The vertical scale of the K-H instability is small and usually appears on
480 the isopycnal. On the one hand, K-H instability weakens the density gradient so that the reflected
481 seismic wave energy is reduced. On the other hand, the vertical scale of K-H instability is lower
482 than the seismic wave resolution (a quarter of the seismic wave wavelength), so it makes overlapped
483 wavelets and stretched wavelength (Figure 9). Therefore, the reflection event in this area is thicker.
484 Besides, the horizontal scale of the K-H instability train is large, which may explain the larger
485 turbulence subrange on the horizontal slope spectrum (Figure 7b).

486

487
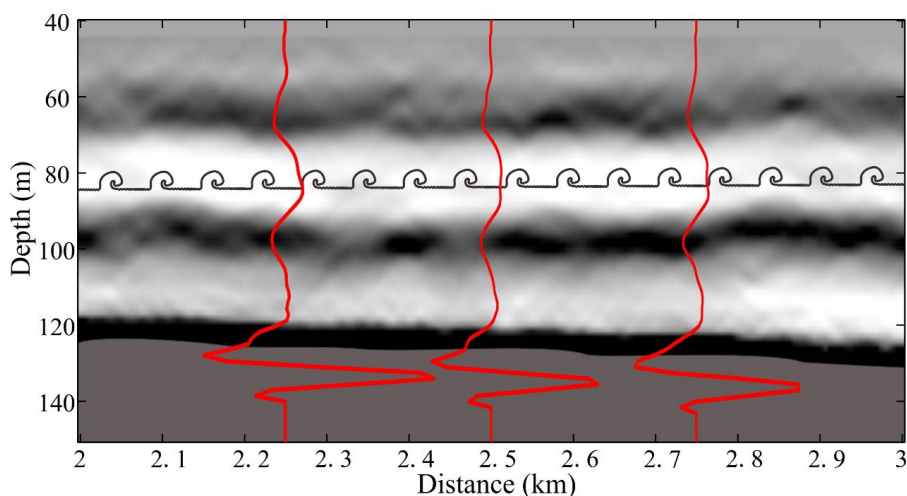
Figure 9. Schematic of the K-H instability. The red lines are the seismic waves, and the black billows represent the K-H instability.

4.2 Enhanced diapycnal mixing induced by the polarity reversal of internal solitary waves

Strong mixing in the ocean mainly occurs near rough topography or area with strong tides (Simpson et al., 1996; Rippeth et al., 2001, 2003; Nash and Moum, 2001; Klymak et al., 2008; Jarosz et al., 2013; Staalstrøm et al., 2015; Wijesekera et al., 2020; Voet et al., 2020). The Dongsha Atoll region in the South China Sea possesses both above features. On one hand, the Dongsha Atoll lies on the continental slope with variable topography. On the other hand, large amplitude internal solitary waves (Alford et al., 2015) propagating from the Luzon Strait reflect, refract, and shoal in this region. This process will dissipate most of the energy carrying by the internal solitary waves. Especially in the shoaling process, polarity reversal and breaking occur and the energy of internal solitary waves transfer to smaller-scale waves. Our results (Figure 6) indicate that the average diffusivity has the magnitude order of O(-4)-O(-3), consistent with previous observations by other techniques. St. Laurent (2008) observed turbulent mixing on the continental shelf and slope, and found that the mixing is higher at the shelf break, and the magnitude order of average dissipation is O(-7)-O(-6).

According to the average buoyancy frequency $N = 6 cph$, the magnitude order of the average diffusivity is O(-4)-O(-3) and consistent with our result. Yang et al. (2014) observed diapycnal mixing on the continental shelf and slope, and found that the average diffusivity can reach the magnitude order of O(-3) too. Similar results have been reported in the study of internal solitary waves shoaling in other regions. For example, Sandstrom et al. (1989) observed the turbulent diffusivity caused by the nonlinear internal wave group on the continental slope of Canada, and found the average diffusivity of 2.4×10^{-3} m²/s. Carter et al. (2005) observed the elevation internal solitary waves in Monterey Bay and a diffusivity on the magnitude order of O(-4). Richards et al. (2013) observed the shoaling of nonlinear internal waves at the St. Lawrence Estuary, which induced high turbulence and enhanced mixing. Therefore, it is reasonable that diapycnal mixing induced by nonlinear internal waves on the continental shelf and slope in the northern South China Sea can

516   reach 100 times that in the open ocean.

517

518   The high diffusivity is mainly in the leading internal solitary wave during the polarity reversal. We
519   suggest that strong mixing may be caused by internal wave breaking due to convective instability.
520   In Figures 8a and 8c, the reflection seismic events are obviously discontinuous in the high
521   turbulence area of the leading wave, indicating that the density gradient is weakened by internal
522   wave breaking. The trough of the internal solitary wave decelerates first when the polarity is
523   reversed (Shroyer et al., 2008), which makes the Froude number (Fr) greater than 1 and causes
524   convective instability. This phenomenon can be found in other observational data. In the high-
525   frequency acoustic section, the backscatter at the top of internal solitary wave is increased when it
526   changes from depression to elevation wave (Orr and Mignerey, 2003), which indicates that the
527   turbulence of the front increased. However, in the seismic section of Figure 8b, we did not find the
528   events break at the front the polarity reversal internal solitary wave. The strong mixing of this
529   internal solitary wave may be induced by shear instability (Figure 9). Therefore, both convective
530   instability and shear instability are responsible for the enhanced mixing in this process. In addition,
531   the non-polarity reversal region in Figure 8a has a higher diffusivity in 50-150 m than other regions.
532   This range is in the thermocline (Figure 1c). The internal waves usually greatly increase mixing in
533   the thermocline, which is related to the shear instability of internal waves (Mackinnon and Gregg,
534   2003). Shear instability is an important mechanism of internal wave dissipation (Farmer and Smith,
535   1978), and it more likely occurs in nonlinear internal waves than convective instability (Zhang and
536   Alford, 2014). The results of high-frequency acoustic observations show that the enhanced
537   backscatter at the bottom of the thermocline represents higher shear instability when the internal
538   solitary waves are shoaling (Orr and Mignerey, 2003), which is consistent with the depth range of
539   high diffusivity in our results.

540

541   What is inconsistent with the observed distribution of mixing is that our results are not able to show
542   diffusivity in the bottom boundary layer. Because our seismic data was collected in summer, the
543   strong stratification at this time limits the vertical range of the bottom boundary layer (Mackinnon
544   and Gregg, 2003). So that the bottom boundary layer near the Dongsha Atoll is thin and lower than
545   the thickness that can be recorded by seismic data. So, the diffusivity we calculated does not include
546   the bottom boundary layer. The enhanced diapycnal mixing induced by the polarity reversal of
547   internal solitary waves plays an important role in local environment and primary productivity. On
548   one hand, diapycnal mixing on the continental slope and shelf makes an important contribution to
549   ocean heat flux, which affects climate and the ocean through heat exchange of local water column
550   (Rahmstorf, 2003; Tian et al., 2009). On the other hand, the vertical flux caused by turbulence can
551   redistribute materials in the ocean and have an important impact on the marine ecological
552   environment (Sharples et al., 2001; Moum et al., 2003; Klymak and Moum, 2003; Wang et al., 2007).

553

554   **4.3 The mixing scheme of internal solitary wave shoaling**

555

556   We compared the vertical distribution of diffusivity with the vertical mixing scheme of internal
557   wave breaking proposed by Vlasenko and Huntter (2002). Although Klymak and Legg (2010) also
558   proposed a mixing scheme for internal wave shoaling and achieved good results in numerical
559   simulation, we cannot use this method to calculate mixing parameters because of lacking high

560 resolution density observation data. Figure 10 shows the vertical distribution of diffusivity from

561 seismic data (solid line) and the diffusivity calculated from mixing scheme (dashed line) at 4

562 positions of the three survey lines (black arrows in Figure 8). The reflection events in the L3 section

563 are broken, and it cannot be guaranteed that the events are parallel to the streamline. Therefore, we

564 did not use the method described in section 2.3 to calculate the wave-induced velocity, and thus did

565 not obtain the diffusivity of the mixing scheme. It can be seen from Figure 10 that the turbulent

566 diffusivity gradually decreases from shallow to deep water. Except for the local low diffusivity value

567 in the deep water at the position D of Figure 10b and 10c, the diffusivity reduction rate at the other

568 location is similar. Figures 10a and 10b show that the parameterized diffusivity is nearly 2--3 orders

569 of magnitude smaller than our result, but they have a similar trend of change. In Figure 10a (line

570 L1), the parameterized diffusivity (blue dotted line) at position B decreases an order of magnitude

571 within 50-100 m. This tendency is same as our results. However, the parameterized diffusivity

572 within 150-200 m increases by one order of magnitude, which is inconsistent with our results (solid

573 blue line). The parameterized diffusivity at position C fluctuates periodically and also keeps a

574 decreasing trend on the whole. In the survey line L2, we selected position A and position B to

575 calculate the parameterized diffusivity. The diffusivity at position A (red dashed line) decreases

576 rapidly within 60-100 m, and then almost keeps unchanged. This is different from our result (solid

577 red line), and the reduction rate of the diffusivity is larger than our result. The trend of the diffusivity

578 at position B (blue dashed line) above 110 m is consistent with our results (solid blue line), but the

579 diffusivity below 110 m decreases rapidly and then rises again. In our results, the diffusivity

580 decreases slowly at the same depth. The value is consistent with that in the open ocean. However,

581 the mixing enhanced obviously on the continental shelf and slope, because of the internal wave

582 shoaling. The mixing scheme underestimates mixing, especially the strong mixing induced by the

583 polarity reversal of internal solitary waves. Our results indicate that near the Dongsha Atoll, where

584 large amplitude internal solitary waves develop, mixing will be enhanced by the shoaling internal

585 solitary waves. The diffusivity gradually decreases from shallow to deep water (not including the

586 bottom boundary layer). This has important implications for improving the mixing scheme for

587 models on the continental shelf and slope.

588
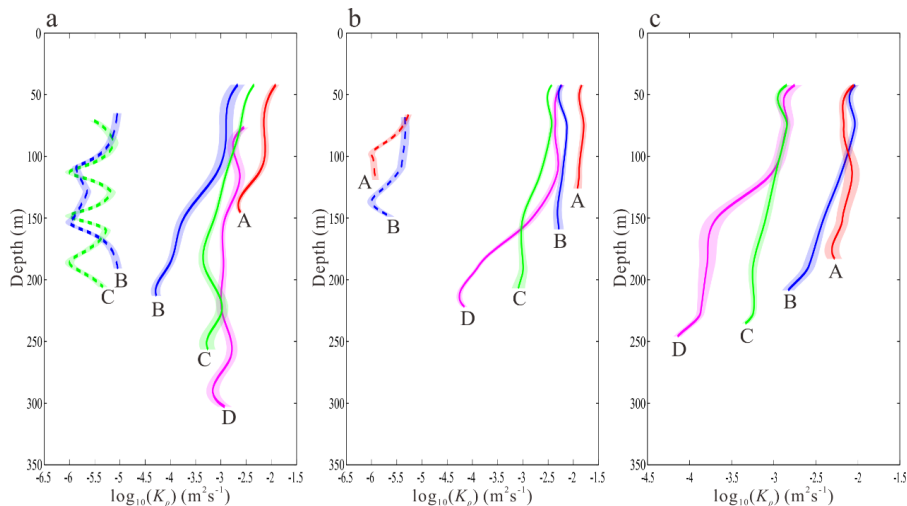
589

590 Figure 10. The vertical distribution of diffusivity from seismic data compare with the mixing scheme.
591 The solid line represents the vertical distribution of diffusivity at the four positions A (red), B (blue), C
592 (green) and D (magenta), and the dotted line represents the parameterized diffusivity at the corresponding
593 positions. The shadow indicates the margin of error.
594
595 **5. Conclusions**
596
597 We have observed the polarity reversal of internal solitary waves by reflection seismic data near the
598 Dongsha Atoll in the South China Sea, and calculated their slope spectra (Figure 6) and diapycnal
599 diffusivity (Figure 8). The results show that the average diapycnal diffusivities of the three survey
600 lines are about two orders of magnitude greater than the open-ocean value. We calculated the
601 average spectral slope of the polarity reversal and non-polarity-reversal regions (Figure 7), and
602 found that the former is about 3 times larger than the latter. The diffusivity maps reveal that
603 horizontally high diffusivity is mainly in the leading wavefront of an internal solitary wave in
604 reversing polarity, and vertically high diffusivity is mainly in the thermocline (50-100 m).
605
606 We analyzed the relation between reflection seismic events and diapycnal diffusivity. The result
607 indicates that continuous and clear reflection events correspond to low diffusivity, while
608 discontinuous or fuzzy events correspond to high diffusivity. The strength of the events also affect
609 the magnitude of diffusivity. The stronger the fluctuation, the higher the spectral energy, and the
610 higher the diffusivity. In addition, we observed an area of high diffusivity with a large horizontal
611 scale in L2, and the reflection events did not appear to be discontinuous or fuzzy. We suggest that
612 this is enhanced mixing induced by the K-H instability (Figure 9). The vertical scale of the K-H
613 instability is smaller than the resolution of our seismic data, so we cannot observe clearly in the
614 seismic data. But its high-energy characteristics can be recorded by reflection events.
615
616 Our results show that shoaling internal solitary wave enhance local mixing. The magnitude order of
617 diapycnal diffusivity is consistent with previous studies. We suggest that there are two mechanisms
618 accounting for the enhanced mixing. On one hand, the polarity reversal of internal solitary waves
619 results in convection instability, which induces internal solitary wave breaking. This mechanism
620 appears at the leading edge of one internal solitary wave in the survey lines L1 and L3. The
621 discontinuous reflection events indicate that the internal solitary wave is broken. While in the
622 seismic section of L2, the reflection events are continuous and clear at the leading edge of the
623 internal solitary wave and other strong mixing areas in the three sections. Such strong mixing is
624 mainly caused by shear instability.
625
626 We picked four positions from the diffusivity maps to analyze the vertical distribution of diapycnal
627 diffusivity (Figure 10).Our result shows that the diffusivity gradually decreased from shallow to
628 deep water (excluding the bottom boundary layer). Compared with previous one mixing scheme,
629 the parameterized diffusivity is about 2--3 orders of magnitude smaller than our result. This means
630 that the mixing scheme underestimates mixing induced by internal solitary wave shoaling near the
631 Dongsha Atoll. However, the vertical pattern of the parameterized diffusivity is consistent with our
632 result.
633

Author contribution. The concept of this study was developed by Haibin Song and extended upon by all involved. Yi Gong implemented the study and performed the analysis with guidance from Haibin Song. Zhongxiang Zhao, Yongxian Guan, Kun Zhang, Yunyan Kuang and Wenhao Fan collaborated in discussing the results and composing the manuscript.

Competing interests. The authors declare that they have no conflict of interest.

References

Alford, M. H., Peacock, T., MacKinnon, J. A., Nash, J. D., Buijsman, M. C., Centurioni, L. R., Chao, S. -Y., Chang, M. -H., Farmer, D. M., Fringer, O. B., Fu, K. -H., Gallacher, P. C., Graber, H. C., Helfrich, K. R., Jachec, S. M., Jackson, C. R., Klymak, J. M., Ko, D. S., Jan, S., Shaun Johnston, T. M., Legg, S., Lee, I. -H., Lien, R. -C., Mercier, M. J., Moum, J. N., Musgrave, R., Park, J. -H., Pickering, A. I., Pinkel, R., Rainville, L., Ramp, S. R., Rudnick, D. L., Sarkar, S., Scotti, A., Simmons, H. L., St Laurent, L. C., Venayagamoorthy, S. K., Wang, Y. -H., Wang, J., Yang, Y. J., Paluszkiewicz, T., and Tang, T. -Y.: The formation and fate of internal waves in the South China Sea, Nature, 521, 65-69, https://doi.org/10.1038/nature14399, 2015.

Bai, Y., Song, H., Guan, Y., and Yang, S.: Estimating depth of polarity conversion of shoaling internal solitary waves in the northeastern South China Sea, Continental Shelf Research, 143, 9-17, https://doi.org/10.1016/j.csr.2017.05.014, 2017.

Bogucki, D., Dickey, T., and Redekopp, L. G.: Sediment resuspension and mixing by resonantly generated internal solitary waves, Journal of Physical Oceanography, 27, 1181-1196, https://doi.org/10.1175/1520-0485(1997)027<1181:SRAMBR>2.0.CO;2, 1997.

Bourgault, D., Blokhina, M. D., Mirshak, R., and Kelley, D. E.: Evolution of a shoaling internal solitary wavetrain, Geophysical Research Letters, 34, https://doi.org/10.1029/2006gl028462, 2007.

Cai, S., Xie, J., and He, J.: An overview of internal solitary waves in the South China Sea, Surveys in Geophysics, 33, 927-943, https://doi.org/10.1007/s10712-012-9176-0, 2012.

Carter, G. S., Gregg, M. C., and Lien, R. -C.: Internal waves, solitary-like waves, and mixing on the Monterey Bay shelf, Continental Shelf Research, 25, 1499-1520, https://doi.org/10.1016/j.csr.2005.04.011, 2005.

Chang, M.-H., Jheng, S.-Y., and Lien, R.-C.: Trains of large Kelvin-Helmholtz billows observed in the Kuroshio above a seamount, Geophysical Research Letters, 43, 8654-8661,

678   https://doi.org/10.1002/2016gl069462, 2016.

679   Chang, M.-H., Lien, R.-C., Tang, T. Y., D'Asaro, E. A., and Yang, Y. J.: Energy flux of nonlinear
680   internal waves in northern South China Sea, Geophysical Research Letters, 33,
681   https://doi.org/10.1029/2005gl025196, 2006.

682   Dickinson, A., White, N. J., and Caulfield, C. P.: Spatial variation of diapycnal diffusivity estimated
683   from seismic imaging of internal wave field, Gulf of Mexico, Journal of Geophysical Research:
684   Oceans, 122, 9827-9854, https://doi.org/10.1002/2017jc013352, 2017.

685   Fan, W., Song, H., Gong, Y., Sun, S., Zhang, K., Wu, D., Kuang, Y., and Yang, S.: The shoaling mode-2
686   internal solitary waves in the Pacific coast of Central America investigated by marine seismic survey
687   data, Continental Shelf Research, 212, 104318, https://doi.org/10.1016/j.csr.2020.104318, 2021.

688   Fortin, W. F. J., Holbrook, W. S., and Schmitt, R. W.: Mapping turbulent diffusivity associated with
689   oceanic internal lee waves offshore Costa Rica, Ocean Science, 12, 601-612,
690   https://doi.org/10.5194/os-12-601-2016, 2016.

691   Gregg, M. C. and Özsoy, E.: Mixing on the Black Sea Shelf north of the Bosphorus, Geophysical
692   Research Letters, 26, 1869-1872, https://doi.org/10.1029/1999gl900431, 1999.

693   Grimshaw, R., Pelinovsky, E., Talipova, T., and Kurkina, O.: Internal solitary waves: propagation,
694   deformation and disintegration, Nonlinear Processes in Geopysics, 17, 633-649,
695   https://doi.org/10.5194/npg-17-633-2010, 2010.

696   Haren, H. v., Gostiaux, L., Morozov, E., and Tarakanov, R.: Extremely long Kelvin-Helmholtz billow
697   trains in the Romanche Fracture Zone, Geophysical Research Letters, 41, 8445-8451,
698   https://doi.org/10.1002/2014GL062421, 2014.

699   Holbrook, W. S., Pa´ramo, P., Pearse, S., and Schmitt, R. W.: Thermohaline fine structure in an
700   oceanographic front from seismic reflection profiling, Science, 301, 821-824,
701   https://doi.org/10.1126/science.1085116, 2003.

702   Holbrook, W. S., Fer, I., Schmitt, R. W., Lizarralde, D., Klymak, J. M., Helfrich, L. C., and Kubichek,
703   R.: Estimating oceanic turbulence dissipation from seismic images, Journal of Atmospheric and
704   Oceanic Technology, 30, 1767-1788, https://doi.org/10.1175/jtech-d-12-00140.1, 2013.

705   Holloway, P. E.: A regional model of the semidiurnal internal tide on the Australian North West Shelf,
706   Journal of Geophysical Research: Oceans, 106, 19625-19638, https://doi.org/10.1029/2000jc000675,
707   2001.

708   Holloway, P. E., Pelinovsky, E., and Talipova, T.: A generalized Korteweg-de Vries model of internal
709   tide transformation in the coastal zone, Journal of Geophysical Research: Oceans, 104, 18333-
710   18350, https://doi.org/10.1029/1999jc900144, 1999.

711   Jarosz, E., Teague, W. J., Book, J. W., and Beşiktepe, Ş. T.: Observed volume fluxes and mixing in the
712   Dardanelles Strait, Journal of Geophysical Research: Oceans, 118, 5007-5021,
713   https://doi.org/10.1002/jgrc.20396, 2013.

714   Klymak, J. M. and Legg, S. M.: A simple mixing scheme for models that resolve breaking internal
715   waves, Ocean Modelling, 33, 224-234, https://doi.org/10.1016/j.ocemod.2010.02.005, 2010.

716   Klymak, J. M. and Moum, J. N.: Internal solitary waves of elevation advancing on a shoaling shelf,
717   Geophysical Research Letters, 30, n/a-n/a, https://doi.org/10.1029/2003gl017706, 2003.

718   Klymak, J. M. and Moum, J. N.: Oceanic isopycnal slope spectra. Part II: Turbulence, Journal of
719   Physical Oceanography, 37, 1232-1245, https://doi.org/10.1175/jpo3074.1, 2007.

720   Klymak, J. M., Pinkel, R., and Rainville, L.: Direct breaking of the internal tide near topography:
721   Kaena Ridge, Hawaii, Journal of Physical Oceanography, 38, 380-399,

722   https://doi.org/10.1175/2007jpo3728.1, 2008.

723   Klymak, J. M., Pinkel, R., Liu, C.-T., Liu, A. K., and David, L.: Prototypical solitons in the South
724   China Sea, Geophysical Research Letters, 33, https://doi.org/10.1029/2006gl025932, 2006.

725   Kunze, E.: Internal-wave-driven mixing: global geography and budgets, Journal of Physical
726   Oceanography, 47, 1325-1345, https://doi.org/10.1175/jpo-d-16-0141.1, 2017.

727   Lee, C. M., Sanford, T. B., Naveira Garabato, A. C., Waterman, S., Fer, I., Carter, G. S., Huussen, T. N.,
728   Whalen, C. B., Talley, L. D., Pinkel, R., Sun, O. M., St. Laurent, L. C., Polzin, K. L., Simmons, H.
729   L., Kunze, E., Alford, M. H., Nash, J. D., MacKinnon, J. A., and Waterhouse, A. F.: Global patterns
730   of diapycnal mixing from measurements of the turbulent dissipation rate, Journal of Physical
731   Oceanography, 44, 1854-1872, https://doi.org/10.1175/jpo-d-13-0104.1, 2014.

732   Lien, R. C., Tang, T. Y., Chang, M. H., and D'Asaro, E. A.: Energy of nonlinear internal waves in the
733   South China Sea, Geophysical Research Letters, 32, https://doi.org/10.1029/2004gl022012, 2005.

734   Liu, A. K., Chang, Y. S., Hsu, M.-K., and Liang, N. K.: Evolution of nonlinear internal waves in the
735   East and South China Seas, Journal of Geophysical Research: Oceans, 103, 7995-8008,
736   https://doi.org/10.1029/97jc01918, 1998.

737   MacKinnon, J. A. and Gregg, M. C.: Mixing on the late-summer new England shelf—solibores, shear,
738   and stratification, Journal of Physical Oceanography, 33, 1476-1492, https://doi.org/10.1175/1520-
739   0485(2003)033<1476:MOTLNE>2.0.CO;2, 2003.

740   Masunaga, E., Arthur, R. S., and Fringer, O. B.: Internal wave breaking dynamics and associated
741   mixing in the Coastal Ocean, 548-554, https://doi.org/10.1016/b978-0-12-409548-9.10953-4, 2019.

742   Mojica, J. F., Sallarès, V., and Biescas, B.: High-resolution diapycnal mixing map of the Alboran Sea
743   thermocline from seismic reflection images, Ocean Science, 14, 403-415, https://doi.org/10.5194/os-
744   14-403-2018, 2018.

745   Moum, J., N, Farmer, D., M, Smyth, W., D, Armi, L., and Vagle, S.: Structure and generation of
746   turbulence at interfaces strained by internal solitary waves propagating shoreward over the
747   continental shelf, Journal of Physical Oceanography, 33, 2093-2112, https://doi.org/10.1175/1520-
748   0485(2003)033<2093:SAGOTA>2.0.CO;2, 2003.

749   Moum, J. N., Farmer, D. M., Shroyer, E. L., Smyth, W. D., and Armi, L.: Dissipative losses in
750   nonlinear internal waves propagating across the Continental Shelf, Journal of Physical
751   Oceanography, 37, 1989-1995, https://doi.org/10.1175/jpo3091.1, 2007a.

752   Moum, J. N., Klymak, J. M., Nash, J. D., Perlin, A., and Smyth, W. D.: Energy transport by nonlinear
753   internal waves, Journal of Physical Oceanography, 37, 1968-1988, https://doi.org/10.1175/jpo3094.1,
754   2007b.

755   Nakamura, Y., Noguchi, T., Tsuji, T., Itoh, S., Niino, H., and Matsuoka, T.: Simultaneous seismic
756   reflection and physical oceanographic observations of oceanic fine structure in the Kuroshio
757   extension front, Geophysical Research Letters, 33, https://doi.org/10.1029/2006gl027437, 2006.

758   Nandi, P., Holbrook, W. S., Pearse, S., Páramo, P., and Schmitt, R. W.: Seismic reflection imaging of
759   water mass boundaries in the Norwegian Sea, Geophysical Research Letters, 31, 345-357,
760   https://doi.org/10.1029/2004GL021325, 2004.

761   Nash, J. D. and Moum, J. N.: Internal hydraulic flows on the continental shelf High drag states over a
762   small bank, Journal of Geophysical Research, 106, 4593-4611,
763   https://doi.org/10.1029/1999JC000183, 2001.

764   Orr, M. H. and Mignerey, P. C.: Nonlinear internal waves in the South China Sea: Observation of the
765   conversion of depression internal waves to elevation internal waves, Journal of Geophysical

Nonlinear Processes
in Geophysics
Discussions
Open Access
EGU

766   Research, 108, https://doi.org/10.1029/2001jc001163, 2003.

767   Osborn, T. R.: Estimates of the local rate of vertical diffusion from dissipation measurements, Journal

768   of Physical Oceanography, 10, 83-89, https://doi.org/10.1175/1520-

769   0485(1980)010<0083:Eotlro>2.0.Co;2, 1980.

770   Pacanowski, R. and Philander, S.: Parameterization of vertical mixing in numerical models of tropical

771   oceans, Journal of Physical Oceanography, 11, 1443-1451, https://doi.org/10.1175/1520-

772   0485(1981)011<1443:povmin>2.0.co;2, 1981.

773   Palmer, M. R., Inall, M. E., and Sharples, J.: The physical oceanography of Jones Bank: A mixing

774   hotspot in the Celtic Sea, Progress in Oceanography, 117, 9-24,

775   https://doi.org/10.1016/j.pocean.2013.06.009, 2013.

776   Ramhstorf, S.: Thermohaline circulation: The current climate, Nature, 421, 699,

777   https://doi.org/10.1038/421699a, 2003.

778   Richards, C., Bourgault, D., Galbraith, P. S., Hay, A., and Kelley, D. E.: Measurements of shoaling

779   internal waves and turbulence in an estuary, Journal of Geophysical Research: Oceans, 118, 273-286,

780   https://doi.org/10.1029/2012jc008154, 2013.

781   Rippeth, T. P., Fisher, N. R., and Simpson, J. H.: The cycle of turbulent dissipation in the presence of

782   tidal straining, journal of Physical Oceanography, 31, 2458–2471, https://doi.org/10.1175/1520-

783   0485(2001)031<2458:TCOTDI>2.0.CO;2, 2001.

784   Rippeth, T. P., Simpson, J. H., Williams, E., and Inall, M. E.: Measurement of the rates of production

785   and dissipation of turbulent kinetic energy in an energetic tidal flow Red Wharf Bay revisited,

786   Journal of Physical Oceanography, 33, 1889–1901, https://doi.org/10.1175/1520-

787   0485(2003)033<1889:MOTROP>2.0.CO;2, 2003.

788   Ruddick, B., Song, H., Dong, C., and Pinheiro, L.: Water column seismic images as maps of

789   temperature gradient, Oceanography, 21, 192-205, https://doi.org/10.5670/oceanog.2009.19, 2009.

790   Sallarès, V., Mojica, J. F., Biescas, B., Klaeschen, D., and Gràcia, E.: Characterization of the

791   submesoscale energy cascade in the Alboran Sea thermocline from spectral analysis of high-

792   resolution MCS data, Geophysical Research Letters, 43, 6461-6468,

793   https://doi.org/10.1002/2016GL069782, 2016.

794   Sallarès, V., Biescas, B., Buffett, G., Carbonell, R., Dañobeitia, J. J., and Pelegrí, J. L.: Relative

795   contribution of temperature and salinity to ocean acoustic reflectivity, Geophysical Research Letters,

796   36, https://doi.org/10.1029/2009gl040187, 2009.

797   Sandstrom, H. and Oakey, N. S.: Dissipation in internal tides and solitary waves, Journal of Physical

798   Oceanography, 25, 604-614, https://doi.org/10.1175/1520-0485(1995)025<0604:DIITAS>2.0.CO;2,

799   1995.

800   Sandstrom, H., Elliot, J. A., and Cchrane, N. A.: Observing groups of solitary internal waves and

801   turbulence with BATFISH and Echo-Sounder, Journal of Physical Oceanography, 19, 987-997,

802   https://doi.org/10.1175/1520-0485(1989)019<0987:OGOSIW>2.0.CO;2, 1989.

803   Seim, H. E. and Gregg, M. C.: Detailed observations of a naturally occurring shear instability, Journal

804   of Geophysical Research, 99, 10049, https://doi.org/10.1029/94jc00168, 1994.

805   Sharples, J., Moore, C. M., and Abraham, E. R.: Internal tide dissipation, mixing, and vertical nitrate

806   flux at the shelf edge of NE New Zealand, Journal of Geophysical Research: Oceans, 106, 14069-

807   14081, https://doi.org/10.1029/2000jc000604, 2001.

808   Sheen, K. L., White, N. J., and Hobbs, R. W.: Estimating mixing rates from seismic images of oceanic

809   structure, Geophysical Research Letters, 36, https://doi.org/10.1029/2009gl040106, 2009.

810 Shroyer, E., L, Moum, J., N, and Nash, J., D: Observations of polarity reversal in shoaling nonlinear
811   internal waves, Journal of Physical Oceanography, 39, 691-701,
812   http://dx.doi.org/10.1175/2008JPO3953.1, 2008.
813 Simpson, J. H., Crawford, W. R., Rippeth, T. P., Campbell, A. R., and Cheok, J. V. S.: The vertical
814   structure of turbulent dissipation in shelf seas, Journal of Physical Oceanography, 26, 1579–1590,
815   https://doi.org/10.1175/1520-0485(1996)026<1579:TVSOTD>2.0.CO;2, 1996.
816 St Laurent, L., Simmons, H., Tang, T. Y., and Wang, Y.: Turbulent properties of internal waves in the
817   South China Sea, Oceanography, 24, 78-87, https://doi.org/10.5670/oceanog.2011.96, 2011.
818 St. Laurent, L.: Turbulent dissipation on the margins of the South China Sea, Geophysical Research
819   Letters, 35, https://doi.org/10.1029/2008gl035520, 2008.
820 Staalstrøm, A., Arneborg, L., Liljebladh, B., and Broström, G.: Observations of turbulence caused by a
821   combination of tides and mean baroclinic flow over a Fjord Sill, Journal of Physical Oceanography,
822   45, 355-368, https://doi.org/10.1175/jpo-d-13-0200.1, 2015.
823 Terletska, K., Choi, B. H., Maderich, V., and Talipova, T.: Classification of internal waves shoaling
824   over slope-shelf topography, Russian Journal of Earth Science, 20,
825   https://doi.org/10.2205/2020ES000730, 2020.
826 Tian, J., Yang, Q., and Zhao, W.: Enhanced diapycnal mixing in the South China Sea, Journal of
827   Physical Oceanography, 39, 3191-3203, https://doi.org/10.1175/2009jpo3899.1, 2009.
828 Tu, J., Fan, D., Lian, Q., Liu, Z., Liu, W., Kaminski, A., and Smyth, W.: Acoustic observations of
829   Kelvin‑Helmholtz billows on an Estuarine Lutocline, Journal of Geophysical Research: Oceans,
830   125, https://doi.org/10.1029/2019jc015383, 2019.
831 Vlasenko, V. and Hutter, K.: Numerical experiments on the breaking of solitary internal waves over a
832   slope–shelf topography, Journal of Physical Oceanography, 32, 1779-1793,
833   https://doi.org/10.1175/1520-0485(2002)032<1779:NEOTBO>2.0.CO;2, 2002.
834 Voet, G., Alford, M. H., MacKinnon, J. A., and Nash, J. D.: Topographic form drag on tides and low-
835   frequency flow: observations of nonlinear lee waves over a Tall Submarine Ridge near Palau,
836   Journal of Physical Oceanography, 50, 1489-1507, https://doi.org/10.1175/jpo-d-19-0257.1, 2020.
837 Wang, Y.-H., Dai, C.-F., and Chen, Y.-Y.: Physical and ecological processes of internal waves on an
838   isolated reef ecosystem in the South China Sea, Geophysical Research Letters, 34,
839   https://doi.org/10.1029/2007gl030658, 2007.
840 Whalen, C. B., Talley, L. D., and MacKinnon, J. A.: Spatial and temporal variability of global ocean
841   mixing inferred from Argo profiles, Geophysical Research Letters, 39,
842   https://doi.org/10.1029/2012gl053196, 2012.
843 Wijesekera, H. W., Wesson, J. C., Wang, D. W., Teague, W. J., and Hallock, Z. R.: Observations of flow
844   separation and mixing around the Northern Palau Island/Ridge, Journal of Physical Oceanography,
845   50, 2529-2559, https://doi.org/10.1175/jpo-d-19-0291.1, 2020.
846 Xu, Z., Yin, B., Hou, Y., Fan, Z., and Liu, A. K.: A study of internal solitary waves observed on the
847   continental shelf in the northwestern South China Sea, Acta Oceanologica Sinica, 29, 18-25,
848   https://doi.org/10.1007/s13131-010-0033-z, 2010.
849 Yang, Q., Tian, J., Zhao, W., Liang, X., and Zhou, L.: Observations of turbulence on the shelf and slope
850   of northern South China Sea, Deep Sea Research Part I: Oceanographic Research Papers, 87, 43-52,
851   https://doi.org/10.1016/j.dsr.2014.02.006, 2014.
852 Zhang, S. and Alford, M. H.: Instabilities in nonlinear internal waves on the Washington continental
853   shelf, Journal of Geophysical Research: Oceans, 120, 5272-5283,

854   https://doi.org/10.1002/2014jc010638, 2015.

855   Zhao, Z.: Satellite observation of internal solitary waves converting polarity, Geophysical Research

856   Letters, 30, https://doi.org/10.1029/2003gl018286, 2003.